Disentangling the multi-scale effects of sea-surface temperatures on global precipitation: A coupled networks approach

Cite as: Chaos **29**, 063116 (2019); doi: 10.1063/1.5095565
Submitted: 11 March 2019 · Accepted: 31 May 2019 ·
Published Online: 20 June 2019

Nikoo Ekhtiari,[1,2,a)] Ankit Agarwal,[1,3,4] Norbert Marwan,[1] and Reik V. Donner[1,5,b)]

AFFILIATIONS

[1]Potsdam Institute for Climate Impact Research, Telegrafenberg A31, 14473 Potsdam, Germany
[2]Department of Physics, Humboldt University, Newtonstr. 15, 12489 Berlin, Germany
[3]Institute of Earth and Environmental Science, University of Potsdam, Karl-Liebknecht-Str. 24-25, 14476 Potsdam-Golm, Germany
[4]GFZ German Research Centre for Geosciences, Section 5.4: Hydrology, Telegrafenberg, 14473 Potsdam, Germany
[5]Department of Water, Environment, Construction and Safety, Magdeburg–Stendal University of Applied Sciences, Breitscheidstr. 2, 39114 Magdeburg, Germany

[a)]**Electronic addresses:** ekhtiari@pik-potsdam.de and nikoo@physik.hu-berlin.de
[b)]**Electronic mail:** reik.donner@pik-potsdam.de

ABSTRACT

The oceans and atmosphere interact via a multiplicity of feedback mechanisms, shaping to a large extent the global climate and its variability. To deepen our knowledge of the global climate system, characterizing and investigating this interdependence is an important task of contemporary research. However, our present understanding of the underlying large-scale processes is greatly limited due to the manifold interactions between essential climatic variables at different temporal scales. To address this problem, we here propose to extend the application of complex network techniques to capture the interdependence between global fields of sea-surface temperature (SST) and precipitation (P) at multiple temporal scales. For this purpose, we combine time-scale decomposition by means of a discrete wavelet transform with the concept of coupled climate network analysis. Our results demonstrate the potential of the proposed approach to unravel the scale-specific interdependences between atmosphere and ocean and, thus, shed light on the emerging multiscale processes inherent to the climate system, which traditionally remain undiscovered when investigating the system only at the native resolution of existing climate data sets. Moreover, we show how the relevant spatial interdependence structures between SST and P evolve across time-scales. Most notably, the strongest mutual correlations between SST and P at annual scale (8–16 months) concentrate mainly over the Pacific Ocean, while the corresponding spatial patterns progressively disappear when moving toward longer time-scales.

The study of the climate system using complex networks provides new insights into spatiotemporal climate dynamics. Most previous studies have focused on a single climate variable only. Accounting for the multivariate and multiscale nature of climate variability introduces a new challenging perspective that could help improve our understanding of the underlying physical mechanisms. In this study, we focus on the aforementioned two aspects of multiple variables and time-scales contributing to the variability of the climate system and show that cross-variable statistical relations evolve differently at different time-scales. Consideration of this previously widely disregarded factor provides a more explicit picture of scale-dependent covariability patterns among climate variables and their temporal evolution, which might be overlooked when focusing only at the native resolution of existing climate data sets.

I. INTRODUCTION

The mutual interdependence between ocean and atmospheric variability, which is mediated via various different processes, is a key ingredient in global climate dynamics across a vast range of spatial and temporal scales.[1–3] In particular, in the tropics and subtropics coupling between both systems via wind stress, differential

heating and evaporation gives rise to important phenomena such as monsoons or the El Niño–Southern Oscillation (ENSO).[4] Thereby, understanding the interactions between ocean and atmosphere in space and time across scales is of fundamental socioeconomic relevance, including fields like agriculture or risk assessment in the context of the insurance sector. The latter relates mainly to the timing and magnitude of climate extremes like heatwaves, floodings, or droughts, which play a vital role for daily life and prosperity of the society yet are hard to assess due to their strong spatiotemporal heterogeneity.

In this work, we focus on the interdependence between sea-surface temperature (SST) and precipitation (P) as two key variables associated with ocean and atmosphere, respectively. There is a large body of existing studies on the interrelation between these two variables and the possible causes and associated impacts of corresponding extremes. In this context, one key physical mechanism is the exchange of surface fluxes.[5,6] Recent studies suggest that P tends to increase in some approximately linear fashion with increasing SST over the tropical monsoon basins, suggesting a noticeable impact of SST on tropical precipitation.[7] By contrast, in the western North Pacific region, the correlation between local rainfall and SST in the boreal summer is negative, indicating that atmospheric dynamics dominates over oceanic preconditioning in determining the rainfall variability of this region.[8,9] This observation may be explained by the monsoon activity during this season. The summer monsoon brings rainfall, but also leads to SST cooling and, hence, the negative correlation between local rainfall and SST. Trenberth and Shea[8] studied the covariability between surface temperature and P globally and found negative correlations over land but positive correlations over high latitudes. They also concluded that ocean conditions drive the atmosphere. In vast parts of the tropics, higher surface air temperatures are associated with more evaporation and, therefore, precipitation, which can be well observed in the core ENSO region in the eastern-to-central tropical Pacific. In turn, other regions, like the western Pacific during boreal summer, feature negative correlations between SST and P, indicating that atmospheric dynamics mainly determines the surface temperatures of the ocean.[8]

To this end, many recent studies suffer from the fact that they account for variations at multiple time-scales at most in terms of considering seasonal composites. However, this largely neglects the variety of time-scales (from subseasonal to decadal) at which ocean and atmosphere interact via an exchange of energy and matter (in our case, water). In turn, recent developments in the field of nonlinear time series analysis like empirical mode decomposition and functional climate networks have already proven their versatile applicability in studying multivariable climate dynamics at different time-scales.[10–12] Here, we follow up on corresponding recent ideas by combining time series decomposition for SST and P into contributions at different time scales with complex network approaches.

Specifically, in order to disentangle the multiscale interdependence between SST and P globally, we first employ the discrete wavelet transform (DWT), which provides a method to process data at different time-scales.[13–17] This technique allows decomposing the local variability of SST and P individually into contributions with different characteristic time-scales. In order to unveil the corresponding scale-specific spatial interdependence patterns, we employ the concept of functional network analysis,[18–21] the development of which has been motivated by numerous examples of successful applications of complex network approaches across scientific disciplines and to problems of great societal relevance.[22] Here, each grid point of a given climate data set corresponds to a node of a spatially embedded network, and links represent strong statistical associations between the variability observed at the respective grid points.

Previous applications of functional network analysis to climate science have mainly focused on individual climatological fields representing the dynamics of a single variable or atmospheric layer. Recently, a multivariate extension of this framework has been introduced in terms of interdependent or coupled climate networks, which allows studying the spatiotemporal interdependence patterns among two or more variables from a complex network perspective.[23–25] However, a detailed analysis of the multiscale spatial characteristics of two interdependent climate variables has not yet been performed. In turn, given the multiplicity of known (almost periodic to broad-banded irregular) oscillatory variability modes in different atmospheric and ocean variables from intraseasonal [e.g., the Madden-Julian Oscillation (MJO)] over interannual [e.g., North Atlantic Oscillation (NAO) and ENSO] to multidecadal scales [e.g., Pacific Decadal Oscillation (PDO) or Atlantic Multidecadal Oscillation (AMO)], it is pivotal to explicitly account for the associated distinct scales in order to attribute the resulting spatial interdependence patterns to specific climate mechanisms. This is precisely what we attempt in the present study.

The remainder of this paper is organized as follows: Sec. II describes the utilized datasets and methods. The results are presented and discussed in Sec. III. Specifically, we will focus on two key local characteristics of spatially embedded coupled networks—the cross-degree and average cross-link distance—between sea-surface temperatures and precipitation. Both measures are presented as maps as well as zonal and meridional averages. The main results of our study are summarized in Sec. IV.

II. DATA AND METHODS

A. Description of the data

We use global monthly SST and precipitation data for the period of 1979–2015 provided by the US National Oceanic and Atmospheric Administration—Earth System Research Laboratory's Physical Sciences Division (NOAA/OAR/ESRL PSD), which are freely available at https://www.esrl.noaa.gov/psd/. Specifically, we employ the ERSST v3b gridded SST dataset with a spatial resolution of $\Delta\lambda = \Delta\phi = 2^\circ$, and the GPCP version 2.3 global precipitation dataset with a resolution of $\Delta\lambda = \Delta\phi = 2.5^\circ$.

Since our goal is to capture long-term climate variability, monthly averages are generally preferred, because the high-frequency variability of daily data products might blur relevant variability at longer time-scales. As a preprocessing step, we first remove all grid points of SST and P with missing values or gaps, resulting in 9456 (SST) and 10 368 (P) grid points, respectively. In a second step, we calculate the resulting anomaly series for each grid point by subtracting the climatological mean for each month of the year from the respective time series. Note that while the SST data set by definition only covers the oceans (without those parts that have been captured by sea-ice during at least one month of the study period), the P data have global coverage including both oceans and continents.

B. Analysis strategy

In order to justify an appropriate analysis strategy, an initial inspection of the properties of the studied time series is useful. Both SST and P fields have been used in a vast body of climatological studies, and their basic features are therefore well understood. As one important aspect, the empirical frequency distributions of values for each grid point could negatively affect the outcomes of standard time series analysis techniques. In the present case, however, we emphasize that while dealing with a native monthly (instead of daily) resolution of our data sets, some of the most critical concerns are circumvented. On the one hand, deviations from a Gaussian distribution are often interpreted as signatures of nonlinear dynamics.[26–30] However, in the case of monthly SST values, non-Gaussianity plays a relatively minor role as compared to atmospheric variables. On the other hand, precipitation at daily scales is known to suffer from the fact that the distribution presents a combination of an occurrence and an intensity process, which implies many zero values, so that the use of correlation-based analysis methods can lead to severe problems that require sophisticated concepts to cope with.[31] However, at monthly scales, except for desert or semidesert regions as well as their oceanic counterparts, the relative fraction of zeros is greatly reduced in comparison with daily data so that the distributional features become markedly less problematic at this coarser temporal resolution. Taken together, both methodological ingredients of this work—wavelet decomposition and correlation analysis—can be considered relatively weakly affected by the distributional features of the time series under study.

The following two subsections briefly explain the details of the two main ingredients of our analysis framework, wavelet decomposition and functional climate network analysis. Figure 1 presents a schematic view of this approach. Initially, we decompose the monthly SST and P data into their respective contributions at different time-scales (up to decadal scales) using the maximum overlap discrete wavelet transform (see below). Then, we compute the pairwise lag-zero correlation coefficients between the resulting scale-specific variations of each SST grid cell and all considered P grid cells. We repeat this procedure at each time-scale of interest. It is important to highlight that we are mainly interested in the effects of SST on precipitation, i.e., how the SST variability at different scales influences P at different time-scales around the globe. Thus, we do not study here possible effects of P on SST, which we have found to be generally less spatially coherent (not shown). Finally, by defining a global threshold to all cross-correlations between the SST and P fields at each time-scale, we obtain binary adjacency matrices that represent the connectivity structure of a coupled climate network based on which the corresponding network topology can be conveniently studied in terms of selected characteristics.

C. Maximum overlap discrete wavelet transform

We use the Maximum Overlap Discrete Wavelet Transform (MODWT), which is a modification of the classical Discrete Wavelet Transform (DWT).[32–34] MODWT decomposes a time series into different time-scales or frequency bands. The wavelet decomposition

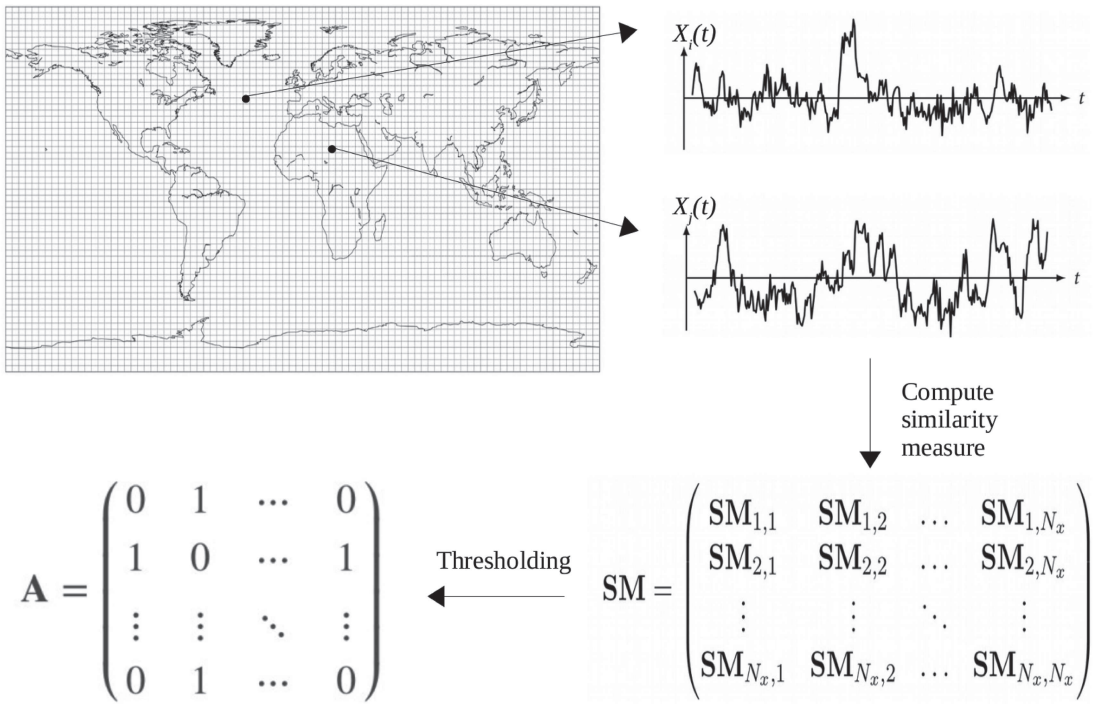

FIG. 1. Schematic illustration of the construction of a functional network from global gridded climate data sets (see text for details). The shown time series excerpts are for illustrative purposes only and do not reflect any of the specific data sets used in the present work.

is realized using two basis functions known as father wavelet and mother wavelet, respectively (see below). Any function $f(t)$ can be expressed through these basis functions and their scaled and translated versions as

$$f(t) = \sum_k s_{J,k}\phi_{J,k}(t) + \sum_k d_{J,k}\Phi_{J,k}(t) + \sum_k d_{J-1,k}\Phi_{J-1,k}(t) + \cdots + \sum_k d_{1,k}\Phi_{1,k}(t), \quad (1)$$

where J is the total number of scales to be analyzed and k is in the range of 1 to T (the length of the time series). The coefficients $s_{J,k}$ are called approximation coefficients and $d_{J,k}, \ldots, d_{1,k}$ wavelet transform coefficients at scales from J to 1, while the functions $\phi_{J,k}(t)$ and $\{\Phi_{j,k}|j = 1, \ldots, J-1, J\}$ are the approximating wavelet function and detail wavelet functions, respectively. These basis functions are defined in terms of father and mother wavelets as follows:

$$\phi_{j,k}(t) = 2^{-\frac{j}{2}}\phi(2^{-j}t - k), \quad (2)$$

$$\Phi_{j,k}(t) = 2^{-\frac{j}{2}}\Phi(2^{-j}t - k). \quad (3)$$

Further, the values of the wavelet transform coefficients at each scale and the approximation coefficients at scale J are estimated by

$$d_{j,k} \approx \int \Phi_{j,k}(t)f(t)dt, \quad j = 1, \ldots, J \quad (4)$$

and

$$s_{J,k} \approx \int \phi_{J,k}(t)f(t)dt, \quad (5)$$

respectively, where the scaling coefficients $s_{J,k}$ capture the smooth trend of the time series at the coarsest scale 2^J (which is why they are also called smooth coefficients), and the wavelet coefficients $d_{j,k}$, also known as detail coefficients, describe fluctuations from the coarsest scale to the finest scale. The original series $f(t)$ can be reconstructed by summing up the detail components and the smooth components as

$$f(t) = S_{J,k} + D_{J,k} + D_{J-1,k} + \cdots + D_{1,k}, \quad (6)$$

where $S_{J,k} = \sum_k s_{J,k}\phi_{J,k}(t)$, $D_{J,k} = \sum_k d_{J,k}\Phi_{J,k}(t)$, and $D_{1,k} = \sum_k d_{1,k}\Phi_{1,k}(t)$. Examples for the resulting decompositions can be vastly found across the literature on geoscientific time series analysis. For two examples of rainfall time series quite similar to those studied in the present work (though with daily resolution), we refer to Fig. 2 of Ref. 35 or Fig. S1 in the supplementary material of Ref. 36.

In this work, we employ the so-called Haar wavelet, a simple piecewise constant function, as a mother and father wavelet. Although its very basic form may be less advantageous for more sophisticated analyses, it considerably simplifies its numerical handling.[35] Notably, Haar wavelets have recently attracted great interest in the context of fluctuation analysis of climate variability.[37]

D. Coupled climate networks

Let us denote the SST and P anomaly fields as $\{X_i(t)\}_{i=1}^{N_i}$ and $\{X_j(t)\}_{j=1}^{N_j}$, respectively, with $t = 1, \ldots, T$ indicating time steps with monthly mean values and i and j the specific grid points on the Earth from which the respective series have been taken. By applying the MODWT, we first decompose each SST and P time series at each grid point into seven distinct time series, each representing a specific time-scale (i.e., 1–2, 2–4, 4–8, 8–16, 16–32, 32–64, and 64–128 months).

For any of these scales, each time series is considered as a node in a climate network, which is identified with the spatial position of the corresponding grid point. Links between node i in the SST field and node j in the P field exist if some similarity measure SM_{ij} between the corresponding time series exceeds a given threshold τ. Thus, the resulting climate network representation is given by the adjacency matrix

$$A_{ij} = \Theta\big(|SM_{ij}| - \tau\big), \quad (7)$$

where $\Theta(\cdot)$ denotes the Heaviside step function. As a similarity measure, we employ the classical Pearson correlation coefficient (PCC) at lag zero as one of the simplest possible statistical association measures. The restriction to this linear characteristic does not contradict the fact that the climate system exhibits a great variety of nonlinear relationships among its components. However, previous works have often shown that the most characteristic network patterns are already well visible in the case of the linear PCC and, thus, do not require the more computationally demanding estimation of nonlinear counterparts like mutual information.[38]

Besides the choice of the similarity measure, the selection of the threshold value τ to distinguish between linked and nonlinked node pairs has to be justified. Some recent studies have systematically addressed the effect of varying values of τ (respectively, the corresponding edge density) on the resulting network measures. While the spatial patterns of node-wise characteristics as exclusively used in this work (see below) commonly show little qualitative variation as the threshold is altered,[21] there are a few exceptions of global characteristics that can be more strongly affected[38] but are not used in this work. Therefore, we do not provide here a thorough investigation of the particular effects of threshold variations in the present context while referring to those previous findings.

To keep only the strongest statistical relationships, we consider τ as the empirical 99% quantile value of all pairwise correlation values at a given MODWT scale. This choice is motivated by recent studies, where it was found that the 99% quantile is adequate for representing atmospheric teleconnections.[38–40] In turn, we do not explicitly account for the increasing autocorrelation of the individual records at coarser time-scales (e.g., by replacing the mutual correlations by associated p-values involving necessary corrections for serial dependency), which originates from the fact that with increasing scale of the MODWT, the signals are gradually smoothed. However, this effect applies to all grid points in a similar way. In what follows, we will exclusively study the statistical linkages between the SST and P fields, while ignoring those between different grid points of the same field (as also considered in previous works[23,25]), making the resulting network representations bipartite graphs where links exist exclusively between nodes (grid points) of different types (variables).

One important point in studying climate networks based on data given on a regular latitude–longitude grid (also called angularly regular grids, as used in this study) is that by moving toward the poles, the spatial density of nodes systematically increases. This can result in some significant bias in the topological characteristics of climate

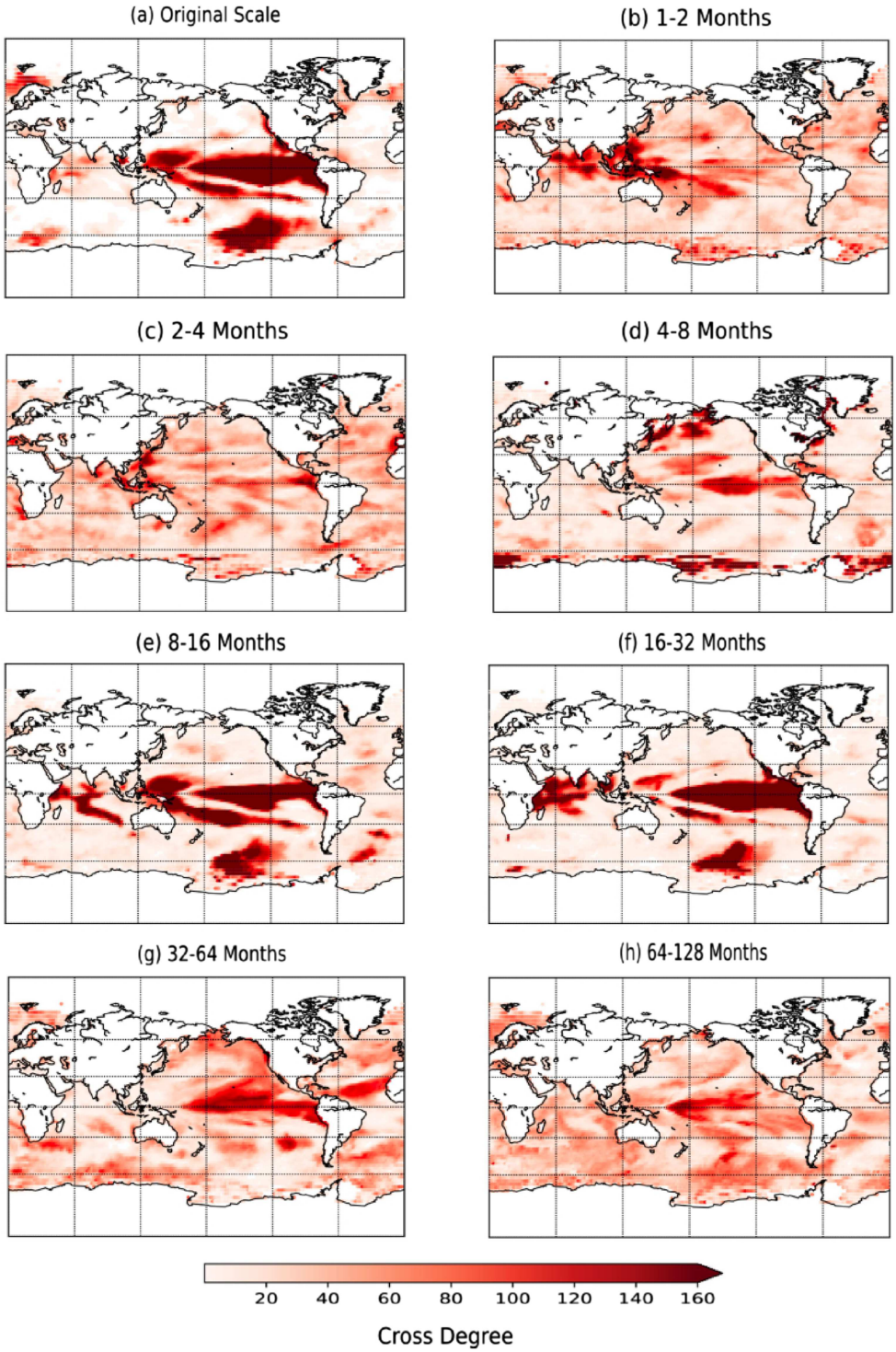

FIG. 2. N.s.i. cross-degree of $SST \rightarrow P$ for (a) the original anomaly time series and (b)–(h) the seven scales obtained by MODWT (1–2, 2–4, 4–8, 8–16, 16–32, 32–64, and 64–128 months), respectively.

networks, since mutually closer nodes are commonly more strongly correlated and, thus, are on average more densely connected in the network. This problem can be accounted for by using specific node-weighted versions of the network measures of interest, so-called *node splitting invariant* (*n.s.i.*) measures.[41] Here, each node is weighted by the area on the Earth's surface it represents so that nodes closer to the poles get gradually lower weights. It can be shown that a proper node weight for angularly regular grids is given by[19]

$$w_q = \cos \lambda_q, \tag{8}$$

where λ_q is the latitude associated with grid point/node q.

Having thus obtained the network's adjacency matrix and introduced proper node weights, we can now estimate different network measures. In this study, we restrict our attention to two characteristics that will be further described in the following. For quantifying local cross-variable interactions, we use the n.s.i. cross-degree,[23,24] which will be complemented by the n.s.i. cross-average link distance which measures the mean spatial distance between any pair of mutually connected (i.e., strongly correlated) SST and P grid points.

1. N.s.i. cross-degree

The n.s.i. cross-degree is defined as

$$k_i = \sum_{j \in V_P} w_j A_{ij} \quad \text{for } i \in V_S, \tag{9}$$

where V_S and V_P denote the sets of nodes of the two subnetworks (here, SST and P) and w_j is the weight of node j as defined in Eq. (8). k_i gives the spatial area represented by those nodes $j \in V_P$ that are connected with a given $i \in V_S$. The opposite direction (i.e., cross-degrees of nodes in the P field into the SST field) can be simply deduced by exchanging the two node sets above, but will not be further discussed in this work.

By studying the n.s.i. cross-degree, we identify which areas of the SST field are strongly correlated with P variations. Those regions in the SST field that exhibit high values of the n.s.i. cross-degree can be interpreted as having particularly strong influence on P anomalies around the globe.

2. N.s.i. cross-average link distance

The second measure of interest in this study is the n.s.i. cross-average link distance

$$ALD_i = \frac{\sum_{j \in V_P} D_{ij} A_{ij}}{k_i} \quad \text{for } i \in V_S, \tag{10}$$

where D_{ij} is the geodesic distance at the Earth's surface between two nodes $i \in V_S$ and $j \in V_P$ that are connected within the two climatological fields. This measure quantifies whether a specific SST node interacts more locally with the nodes of the P field or whether there are long-distance interactions between them.

III. RESULTS AND DISCUSSION

A. Cross-degree at integrated time-scales

Figure 2 shows the spatial pattern of cross-degrees in the SST field with respect to global gridded precipitation data as the link targets. At the original monthly resolution of the data [Fig. 2(a)], it is evident that there are three main SST regions that are characterized by very strong effects on the precipitation field. Two of these regions are located in the equatorial Pacific (eastern-to-central and western tropical Pacific, respectively), while a third one is found in the southern Pacific Ocean.

Regarding the pattern formed by the two tropical regions, it is noticable that these closely resemble the known anomaly patterns of SST and sea-level pressure associated with ENSO. In this context, it should be highlighted that ENSO controls the time-dependent magnitude and spatial extent of the atmospheric Walker circulation over the Pacific, which is responsible for the zonal wind fields transporting moist air from areas with large evaporation (i.e., warm SSTs) to others that are characterized by condensation of water vapor followed by cloud formation and, finally, precipitation. The two areas with high cross-degree coincide with the main region that is directly affected by ENSO, but (especially on longer time scales) also partially by the PDO as a strong mode of Pacific ocean-atmosphere coupled variability at decadal time-scales.

Notably, the spatial centers of action of ENSO and PDO are known to partially overlap. Specifically, while the PDO has its prime center in the Northern Pacific region, it also exhibits considerable covariability patterns in the equatorial Pacific. This is distinctively different from ENSO, which primarily affects climate in the low latitudes, but has less clear linear covariability patterns in the North Pacific,[42] although the existence of corresponding teleconnections has been studied in various papers, e.g., Ref. 43. Taken together, due to their spatial overlap, it is reasonable to consider ENSO and PDO as two mutually interdependent phenomena, which are, however, relatively well separated in terms of their characteristic time scales (with ENSO varying considerably faster than the PDO). The corresponding interactions across space and time are likely mediated via different processes including the so-called Pacific Meridional Mode (PMM).[44,45] In turn, disentangling spatiotemporal SST patterns solely attributable to any of these modes has been proven a challenging task that is a subject of ongoing work.[46] Regarding the results presented in Fig. 2(a), we tentatively conclude that when investigating climate variability at the original (monthly) resolution without separating the effects of different time-scales, the spatial signatures associated with the impacts of ENSO and PDO on global precipitation overlap spatially in the tropical and subtropical Pacific and can thus hardly be distinguished from each other based on the cross-degree pattern alone.

The third SST region with high n.s.i. cross-degree is located in the southern Pacific and appears closely related with the so-called Southern Annular Mode (SAM). Specifically, the spatial position of the identified region coincides well with the Amundsen Sea Low (ASL), a quasistationary atmospheric low pressure system over the Amundsen-Bellingshausen-Ross Sea. Previous works have already demonstrated that the ASL is often intensified or weakened in the presence of different ENSO phases.[47] However, the signatures of different time-scales in the ENSO-ASL teleconnection have hardly

been studied explicitly in previous works, which is why we shall proceed next with considering the cross-degree fields from SST to P at the different frequency bands provided by our MODWT-based time series decomposition.

B. Scale-specific cross-degree patterns

At time-scales of 1–2 months [Fig. 2(b)], the most prominent cross-degree patterns are found in a region comprising the northern Indian Ocean, maritime continent, and westernmost tropical Pacific, implying that SST anomalies in that region have the strongest impacts on global precipitation variability. Both time-scale and spatial signature suggest that these patterns are associated with the MJO, which results in large-scale tropical deep convection patterns propagating eastward and influencing rainfall, especially between the western Indian Ocean and the western-to-central tropical Pacific. The corresponding traveling atmospheric pattern often fades in the eastern tropical Pacific, while eventually reappearing with lower strength over the tropical Atlantic and then reaching again its full strength over the Indian Ocean to complete one of its cycles.

When moving toward slightly larger time-scales [2–4 months, Fig. 2(c)], the aforementioned high cross-degree pattern in the northern Indian and western Pacific oceans is gradually diminished in spatial extent and magnitude. We attribute this to the fact that MJO has no stationary period and, hence, may affect also time-scales beyond 2 months, yet only at its region of strongest effect, which would be compatible with our observations regarding the cross-degree field.

At scales between 4 and 8 months [Fig. 2(d)], we find different high cross-degree regions in the central Pacific ocean, near the Antarctic coastlines and in the northwestern Pacific, as well as some smaller patches along the North American east coast and over the Caribbean. The band around Antarctica is possibly related with the Antarctic Oscillation (AAO) or Southern Annular Mode (SAM),[48] which describes a belt of westerlies related with the oceanic Antarctic Circumpolar Current (ACC) and can have large-scale effects on rainfall over the southern part of Australia,[49] South Africa,[50] and even China.[51] The pattern over the northern Pacific Ocean appears reminiscent to the North Pacific Oscillation (NPO) which primarily acts on subseasonal time-scales.[52] The NPO is characterized by sea-level pressure anomalies that can trigger variations of subtropical SST patterns.[53] The resulting variations in the subtropical SST due to the NPO can in turn affect rainfall over the southern central United States,[52] Mexico,[52] and China.[54] It has been conjectured that NPO can play a vital role in triggering the onset of ENSO phases.[53] This result appears compatible with our observation of an elevated cross-degree pattern in the central Pacific Ocean [Fig. 2(d)], which could be related with such an effect of NPO on ENSO. Note, however, that the analysis presented here is purely correlative and does not aim at providing statements on causal effects among different large-scale patterns, which should be the subject of more detailed follow-up studies.

At scales from 8 to 16 months, we observe high cross-degrees in the eastern-to-central Pacific ocean and a bow-shaped region from the western tropical to central subtropical Pacific. These two patterns closely match the previously discussed regions that are most strongly influenced by the ENSO phenomenon. In addition, we also recover the pattern over the southern Pacific Ocean that can be related to the ASL and its influence on rainfall anomalies over Antarctica.[55] Yet another high cross-degree region emerges over the Indian Ocean, which can be related with the Indian Ocean Dipole (IOD) pattern, an irregular SST oscillation in the western Indian Ocean[56,57] that is known to have marked teleconnections with rainfall patterns around the globe. Specifically, the IOD variability shows negative correlations with the precipitation in southern Western Australia and South Australia,[49] the southern parts of Brazil,[58] and southeast Asia,[59] while positive correlations exist with precipitation over China[60] and south-eastern Africa.[61]

At the scale of 16–32 months [Fig. 2(f)], the cross-degree patterns show strong similarity with those at scales between 8 and 16 months. The most remarkable differences are that the bow-shaped pattern in the Pacific gets much weaker while the western Indian Ocean becomes more prominent. In turn, the patterns in the eastern-to-central equatorial Pacific and the southern Pacific Ocean remain almost the same. It should be noticed that the patterns at both 8–16 and 16–32 months time-scales exhibit the closest similarities with those obtained for the original unfiltered data. This provides evidence that ocean-atmosphere interactions within these two scales (i.e., around the annual cycle period and around two years) are most dominant. The lower frequency contributions most likely result from ENSO, which is known to be the tropical climate variability mode with the highest amplitude of anomalies and most widespread effects globally. In addition, we may speculate about a possible additional effect of the atmospheric quasibiennial oscillation, which has its core frequency right in the identified range of time-scales.

At time-scales of 32–64 months [Fig. 2(g)], the main ENSO-related high cross-degree region in the eastern-to-central tropical Pacific starts to get blurred, while new regions with high cross-degree emerge, especially in the northern tropical to subtropical Atlantic. This pattern could be related to the Atlantic Equatorial Mode (AEM), which describes a quasiperiodic interannual warming and cooling of the equatorial Atlantic SST.[62,63] It has been shown that AEM can affect rainfall over both adjacent and remote regions, including West Africa,[64] Brazil,[65] and even central Europe.[66]

Finally, at 64–128 month time-scales [Fig. 2(h)], we still find elevated cross-degrees over the equatorial and southern Pacific Ocean. Interestingly, the northern Pacific PDO signature that could have been expected to be observable at this time-scale is widely absent in our corresponding results. It may be hypothesized that corresponding patterns could show up only when turning to even lower frequencies. However, given the restricted time coverage of the studied data sets and increasing numerical artefacts of wavelet analyses at the beginning and end of the records, we hesitate to extend the present analysis toward even longer time-scales.

C. Cross-average link distances

Figure 3 shows our results for the cross-average link distance. This measure provides a complementary picture on the strength of the SST–P relationship by unfolding the spatial information contained in the associated coupled network's cross-linkage structure between both fields.

The unfiltered time series [Fig. 3(a)], especially those regions that were already dominant in the n.s.i. cross-degree [Fig. 2(a)], exhibit short cross-link distances (red areas). This indicates that in

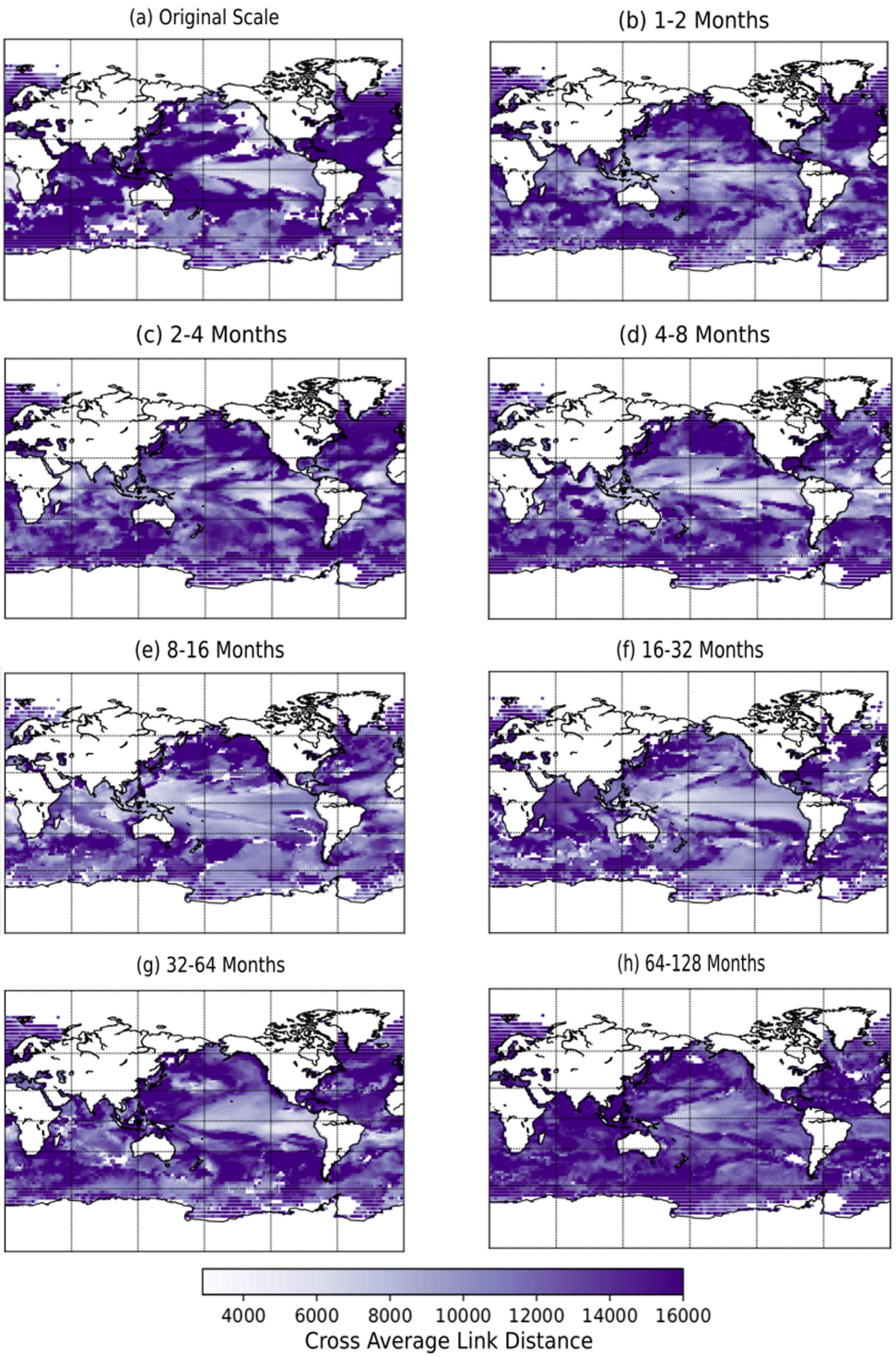

FIG. 3. Same as in Fig. 2, but for the n.s.i. cross-average link distances (in km).

these regions, SST strongly affects P, but mainly at smaller spatial scales, which dominate over possible remote teleconnections.

At time-scales of 1–2 months, most of the tropical oceans show mainly short cross-link distances. This could again be explained by a strong spatially localized modulation of SST and rainfall patterns due to the action of the MJO.

At the scale of 2–4 months, we recall the largely absent high n.s.i. cross-degree patterns that are present at other scales [Fig. 2(c)]. Here, regions with small cross-average link distances only partly coincide with high cross-degrees, while particularly short average cross-link distances are found, e.g., in the eastern Pacific, over Indonesia and in the western part of Indian Ocean [Fig. 3(c)].

For 4–8 month time-scales up to 32–64 months [Figs. 3(d)–3(g)], most of the tropical Pacific previously identified as the most densely connected region in the coupled SST-P network is characterized by short mean cross-link distances, which again points to a dominance of local SST effects on precipitation. In general, this indicates that at smaller spatial scales, SST and precipitation at monthly-to-interannual resolution are most intimately connected in the tropics, where particularly high SSTs imply strong evaporation and, hence, convection feeding predominantly local rainfall. However, we note again that the finding that the tropical oceans are densely connected at short spatial scales does not imply an absence of long-distance connections, but simply a very large amount of short-distance connections.

Beyond these general observations, there are some other regions over which the mean cross-link distances decrease and increase when gradually moving from shorter to longer time-scales. For example, for 4–8 months [Fig. 3(d)], there is a region in the tropical Atlantic with short cross-link distances, which indicate strongly localized cross-correlations between SST and P. Over the western-to-central north Pacific, we find similar short cross-link distances,

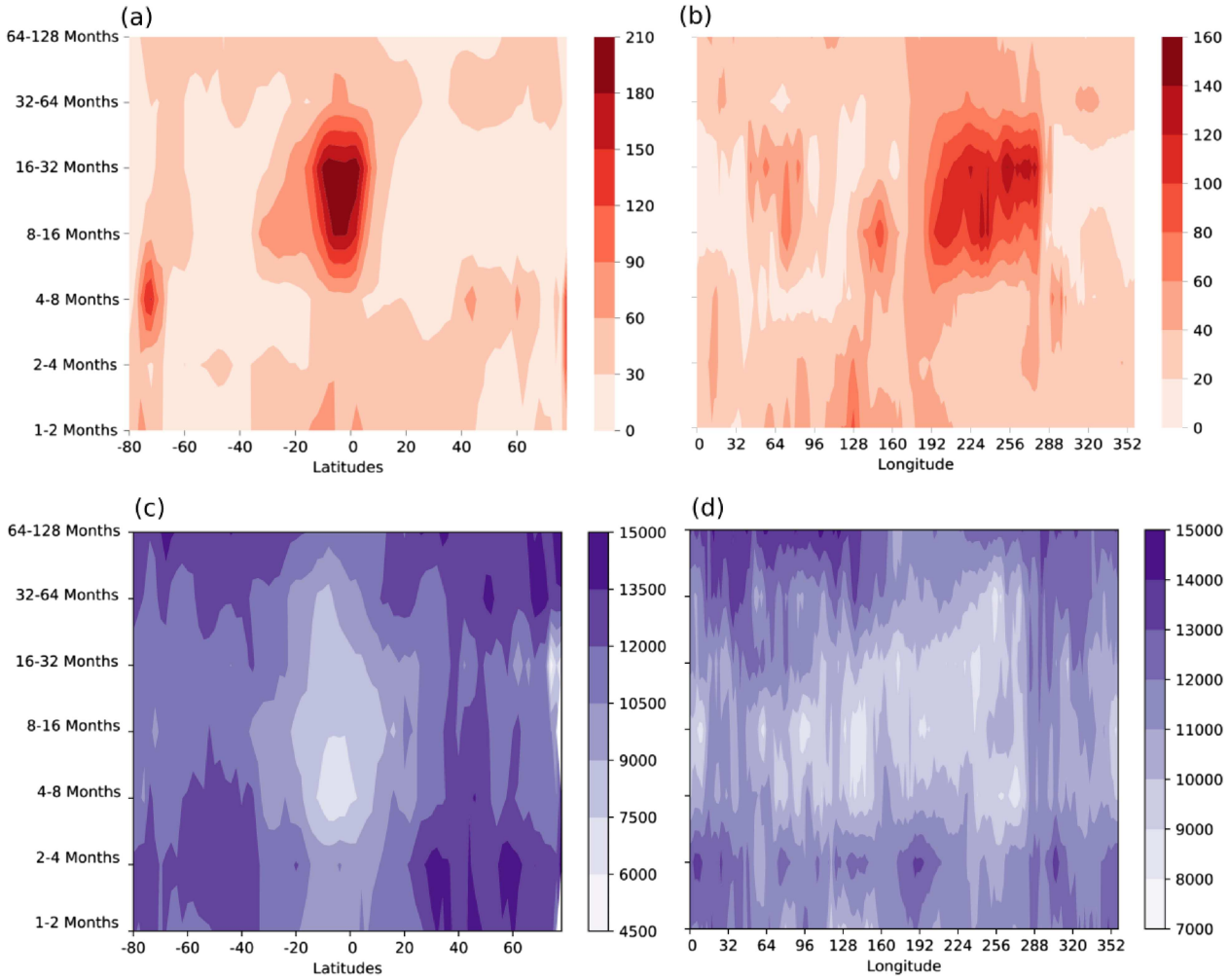

FIG. 4. Average zonal (a) and meridional (b) n.s.i. cross-degree from SST to the global precipitation field. (c) and (d) Same as (a) and (b) but for the n.s.i. cross-average link distance (in km).

which could again be related to the effect of the NPO. By moving toward time-scales of 8–16 months [Fig. 3(e)], the cross-link distances in the tropical Atlantic increase, while those in the eastern Indian ocean decrease as a sign of strongly localized correlations between SST and P in this region. Interestingly, at 16–32 month time-scales [Fig. 3(f)], the cross-link distances over both tropical Atlantic and Indian ocean increase, while only the equatorial Pacific is still characterized by short cross-link distances. This observation could be related to the strong spatial autocorrelation of both SST and precipitation in the ENSO region along with the aforementioned expected SST-precipitation coupling associated with ENSO variability. When proceeding to even longer time-scales of 32–64 months [Fig. 3(g)], the pattern of short cross-link distances in the tropical Pacific shifts toward the eastern part of the equatorial Pacific. Finally, at the time-scale of 64–128 months [Fig. 3(h)], there is only a small region with short cross-link distances remaining in the central tropical Pacific, which—along with the associated cross-degree patterns—indicates a much stronger variety of spatial link placements in the corresponding coupled climate network.

As an important general remark regarding the spatial structure of cross-links as captured by the cross-average link distance, we recall that the precipitation data set has global coverage including both oceans and continents, while the SST data are necessarily spatially limited. Due to the strong interdependence between SST and surface air temperature, a change in SST will strongly affect the atmosphere above the oceans and the resulting amount of water vapor. In turn, our present analysis does not account for the corresponding effect over the continents, which likely has certain implications for the inferred link structures. Future work should, therefore, extend the present analysis by considering the effect of both sea and land surface temperatures (or surface air temperatures) on precipitation using an equivalent analysis strategy.

D. Zonal and meridional mean coupled network properties

In order to summarize the main spatial correlation patterns between ocean and atmosphere at different time-scales as revealed by our coupled networks properties, we finally compute zonal and meridional averages of n.s.i. cross-degree and n.s.i. cross-average link distance over all grid points with available time series. This perspective highlights again the previously found high cross-degrees in the tropics at time-scales between 8–16 and 16–32 months [Fig. 4(a)], primarily in the eastern equatorial Pacific [Fig. 4(b)]. The corresponding results, thus, demonstrate that the effect of SST variations in the eastern equatorial Pacific (i.e., the ENSO region) on global precipitation is generally stronger than in any other ocean basin at annual to shorter interannual time-scales.

Considering the zonal and meridional averages of the n.s.i. cross-average link distance, the tropics are generally characterized by the on average shortest cross-links among all time-scales, while the extratropics generally exhibit longer mean links [Fig. 4(c)]. Taking this information together with the associated cross-degree patterns, it is likely that we observe here mainly regional effects that may originate from temporary SST and precipitation trends reflecting ENSO variability. In turn, some extratropical ocean regions (like the ASL region) also affect global precipitation patterns markedly, yet primarily at larger distances. This could be related to the fact that tropical precipitation reacts more quickly to SST via a fast evaporation–cloud formation–precipitation cycle (e.g., via local convective activity at daily to multiday time-scales), while extratropical influences are transported via the atmospheric circulation (specifically, planetary wave patterns) to remote regions while not having an equally strong local effect on precipitation as tropical SSTs. Taking the longitudinal perspective into account [Fig. 4(d)], we find that localization of interdependence patterns primarily arises on seasonal to interannual time-scales in all three ocean basins, with a focus on the Indian and Pacific Oceans.

In general, our results indicate that the spatial localization properties of ocean-atmosphere interactions as revealed by our analysis are mainly characteristic for the tropics at seasonal to interannual time-scales, while (sub-) seasonal and decadal scales exhibit only few highly and/or short-range connected patterns that are hardly visible in the zonal and meridional averages.

IV. CONCLUSION

We have employed a complex network based framework to investigate the effect of oceanic conditions [expressed via sea-surface temperature (SST) patterns] on global precipitation at time-scales ranging from monthly to decadal scales. For this purpose, we have combined time series decomposition by the maximum overlap discrete wavelet transform with functional network analysis in a coupled network setting.

The observed scale-specific statistical interdependence patterns between our two variables of interest have been characterized by the two coupled network measures n.s.i. cross-degree and n.s.i. cross-average link length. Our analysis reveals main regions of SST that significantly influence precipitation around the globe at different time-scales. Notably, these regions differ among temporal scales, i.e., they show scale-specific behavior. By looking at the raw time series that include variability at all scales, main interdependence patterns between SST and precipitation are found, but information on the associated time-scales cannot be taken into account. Our approach unfolds this otherwise hidden information and allows separating the effects of processes and large-scale climate patterns acting at different characteristic time-scales.

In our case, at their native (monthly) temporal resolution, the two considered climatological fields feature several pronounced spatial patterns that resemble ENSO, PDO, and SAM, which are known to exhibit mutual interdependences. Given the prominent role of ENSO in global climate variability, the dominance of the eastern-to-central tropical Pacific is compatible with expectations. However, other (weaker) atmosphere-ocean covariability features would be easily overlooked in this integral perspective. By decomposing the SST and P time series into distinct time-scales, we are able to trace the appearance and disappearance of different patterns that are related to seasonal over interannual up to decadal variability associated with large-scale climate phenomena. Thereby, we obtain a more explicit picture of other climate modes with different characteristic time-scales that might be important for understanding global precipitation patterns, which is a relevant task in the context of improving future long-term precipitation and drought forecasts.

The substantial variation of the SST-precipitation interdependence globally and across time-scales that is unraveled by the proposed framework provides an exciting perspective for understanding ocean-atmosphere coupling and resulting climate variability. Beyond climate, similar approaches are potentially useful in other fields as well, including neurophysiology[67] or economics, or generally for understanding multicomponent complex systems and their spatiotemporal dynamics.[68]

ACKNOWLEDGMENTS

This study has been financially supported by the German Research Foundation (DFG) via the International Research Training Group IRTG 1740 and the Research Training Group GRK 2043/1 (NatRiskChange), as well as by the German Federal Ministry for Education and Research (BMBF) via the BMBF Young Investigators Group CoSy-CC^2: Complex Systems Approaches to Understanding Causes and Consequences of Past, Present and Future Climate Change (Grant No. 01LN1306A) and the Belmont Forum/JPI Climate project GOTHAM (Grant No. 01LP16MA). Some of the ideas presented in this work have been developed in the course of the bilateral German-Czech project "Spatio-temporal characterization of multiscale and cross-scale atmospheric interactions: Unveiling complex causality patterns for anticipation of future regional climate change" jointly supported by the German Academic Exchange Service (DAAD) and the Academy of Sciences of the Czech Republic under the DAAD Project No. 57154685.

The authors gratefully acknowledge the European Regional Development Fund (ERDF), the German Federal Ministry of Education and Research, and the Land Brandenburg for supporting this project by providing resources on the high performance computer system at the Potsdam Institute for Climate Impact Research. All computations have been performed using the Python package `pyunicorn`.[69]. The author also would like to thank Catrin Kirsch for her comments on the final revision of the paper.

REFERENCES

[1] E. B. Kraus and J. A. Businger, *Atmosphere-Ocean Interaction* (Oxford University Press, 1994).
[2] S. Gadgil, P. V. Joseph, and N. V. Joshi, "Ocean-atmosphere coupling over monsoon regions," Nature **312**, 141–143 (1984).
[3] K. E. Trenberth and J. W. Hurrell, "Decadal atmosphere-ocean variations in the Pacific," Clim. Dyn. **9**(6), 303–319 (1994).
[4] K. E. Trenberth, "The definition of El Niño," Bull. Am. Meteorol. Soc. **78**(12), 2771–2778 (1997).
[5] C. Deser, R. Tomas, M. Alexander, and D. Lawrence, "The seasonal atmospheric response to projected arctic sea ice loss in the late twenty-first century," J. Clim. **23**(2), 333–351 (2010).
[6] A. Agarwal, N. Marwan, R. Maheswaran, B. Merz, and J. Kurths, "Quantifying the roles of single stations within homogeneous regions using complex network analysis," J. Hydrol. (Amst) **563**, 802–810 (2018).
[7] M. K. Roxy, K. Ritika, P. Terray, and S. Masson, "The curious case of Indian Ocean warming," J. Clim. **27**(22), 8501–8509 (2014).
[8] K. E. Trenberth and D. J. Shea, "Relationships between precipitation and surface temperature," Geophys. Res. Lett. **32**(14), L14703, https://doi.org/10.1029/2005GL022760 (2005).
[9] B. Wang, Q. Ding, X. Fu, I.-S. Kang, K. Jin, J. Shukla, and F. Doblas-Reyes, "Fundamental challenge in simulation and prediction of summer monsoon rainfall," Geophys. Res. Lett. **32**(15), L15711, https://doi.org/10.1029/2005GL022734 (2005).
[10] D. Looney, A. Hemakom, and D. P. Mandic, "Intrinsic multi-scale analysis: A multi-variate empirical mode decomposition framework," Proc. R. Soc. Math. Phys. Eng. Sci. **471**(2173), 20140709 (2015).
[11] K. Coughlin and K. K. Tung, "Eleven-year solar cycle signal throughout the lower atmosphere," J. Geophys. Res., [Atmos.] **109**(D21), D21105, https://doi.org/10.1029/2004JD004873 (2004).
[12] K. Steinhaeuser, A. R. Ganguly, and N. V. Chawla, "Multivariate and multiscale dependence in the global climate system revealed through complex networks," Clim. Dyn. **39**(3), 889–895 (2012).
[13] G. A. Bradshaw and B. A. McIntosh, "Detecting climate-induced patterns using wavelet analysis," Environ. Pollut. **83**(1), 135–142 (1994).
[14] K.-M. Lau and H. Weng, "Climate signal detection using wavelet transform: How to make a time series sing," Bull. Am. Meteorol. Soc. **76**(12), 2391–2402 (1995).
[15] N. Jajcay, J. Hlinka, S. Kravtsov, A. A. Tsonis, and M. Paluš, "Time scales of the European surface air temperature variability: The role of the 7–8 year cycle," Geophys. Res. Lett. **43**(2), 902–909, https://doi.org/10.1002/grl.v43.2 (2016).
[16] M. Paluš, "Linked by dynamics: Wavelet-based mutual information rate as a connectivity measure and scale-specific networks," in *Advances in Nonlinear Geosciences*, edited by A. A. Tsonisor (Springer International Publishing, 2018), pp. 427–463.
[17] M. Paluš, "Multiscale atmospheric dynamics: Cross-frequency phase-amplitude coupling in the air temperature," Phys. Rev. Lett. **112**, 078702 (2014).
[18] A. A. Tsonis and P. J. Roebber, "The architecture of the climate network," Physica A **333**, 497–504 (2004).
[19] A. A. Tsonis, K. L. Swanson, and P. J. Roebber, "What do networks have to do with climate?," Bull. Am. Meteorol. Soc. **87**(5), 585–596 (2006).
[20] J. F. Donges, Y. Zou, N. Marwan, and J. Kurths, "The backbone of the climate network," Europhys. Lett. **87**(4), 48007 (2009).
[21] J. F. Donges, Y. Zou, N. Marwan, and J. Kurths, "Complex networks in climate dynamics," Eur. Phys. J. Spec. Top. **174**(1), 157–179 (2009).
[22] D. Helbing, D. Brockmann, T. Chadefaux, K. Donnay, U. Blanke, O. Woolley-Meza, M. Moussaid, A. Johansson, J. Krause, S. Schutte, and M. Perc, "Saving human lives: What complexity science and information systems can contribute," J. Stat. Phys. **158**(3), 735–781 (2015).
[23] J. F. Donges, H. C. H. Schultz, N. Marwan, Y. Zou, and J. Kurths, "Investigating the topology of interacting networks," Eur. Phys. J. B **84**(4), 635–651 (2011).
[24] A. Feng, Z. Gong, Q. Wang, and G. Feng, "Three-dimensional air–sea interactions investigated with bilayer networks," Theor. Appl. Climatol. **109**(3), 635–643 (2012).
[25] M. Wiedermann, J. F. Donges, D. Handorf, J. Kurths, and R. V. Donner, "Hierarchical structures in Northern Hemispheric extratropical winter ocean–atmosphere interactions," Int. J. Climatol. **37**(10), 3821–3836 (2016).
[26] J. M. Peters and S. Kravtsov, "Origin of non-gaussian regimes and predictability in an atmospheric model," J. Atmos. Sci. **69**(8), 2587–2599 (2012).
[27] M. Perron and P. Sura, "Climatology of non-gaussian atmospheric statistics," J. Clim. **26**(3), 1063–1083 (2013).
[28] P. Sura and A. Hannachi, "Perspectives of non-gaussianity in atmospheric synoptic and low-frequency variability," J. Clim. **28**(13), 5091–5114 (2015).
[29] A. Hannachi, D. M. Straus, C. L. E. Franzke, S. Corti, and T. Woollings, "Low-frequency nonlinearity and regime behavior in the northern hemisphere extratropical atmosphere," Rev. Geophys. **55**(1), 199–234, https://doi.org/10.1002/2015RG000509 (2017).
[30] M. Linz, G. Chen, and Z. Hu, "Large-scale atmospheric control on non-gaussian tails of midlatitude temperature distributions," Geophys. Res. Lett. **45**(17), 9141–9149, https://doi.org/10.1029/2018GL079324 (2018).
[31] C. Ciemer, N. Boers, H. M. J. Barbosa, J. Kurths, and A. Rammig, "Temporal evolution of the spatial covariability of rainfall in South America," Clim. Dyn. **51**(1), 371–382 (2018).
[32] M. Rathinasamy, R. Khosa, J. Adamowski, C. Sudheer, G. Partheepan, J. Anand, and B. Narsimlu, "Wavelet-based multiscale performance analysis: An approach to assess and improve hydrological models," Water. Resour. Res. **50**(12), 9721–9737, https://doi.org/10.1002/2013WR014650 (2014).
[33] D. B. Percival, "Analysis of geophysical time series using discrete wavelet transforms: An overview," in *Nonlinear Time Series Analysis in the Geosciences: Applications in Climatology, Geodynamics and Solar-Terrestrial Physics*, edited by R. V. Donner and S. M. Barbosa (Springer, Berlin, 2008), pp. 61–79.

[34]A. Agarwal, R. Maheswaran, N. Marwan, L. Caesar, and J. Kurths, "Wavelet-based multiscale similarity measure for complex networks," Eur. Phys. J. B **91**(11), 296 (2018).
[35]A. Agarwal, N. Marwan, M. Rathinasamy, B. Merz, and J. Kurths, "Multi-scale event synchronization analysis for unravelling climate processes: A wavelet-based approach," Nonlinear Process. Geophys. **24**(4), 599–611 (2017).
[36]J. Kurths, A. Agarwal, N. Marwan, M. Rathinasamy, L. Caesar, R. Krishnan, and B. Merz, "Unraveling the spatial diversity of Indian precipitation teleconnections via nonlinear multi-scale approach," Nonlinear Process. Geophys. Discuss. (to be published).
[37]S. Lovejoy, "Spectra, intermittency, and extremes of weather, macroweather and climate," Sci. Rep. **8**(1), 12697 (2018).
[38]A. Radebach, R. V. Donner, J. Runge, J. F. Donges, and J. Kurths, "Disentangling different types of El Niño episodes by evolving climate network analysis," Phys. Rev. E **88**(5), 052807 (2013).
[39]F. Arizmendi, A. C. Martí, and M. Barreiro, "Evolution of atmospheric connectivity in the 20th century," Nonlinear Process. Geophys. **21**(4), 825–839 (2014).
[40]A. Agarwal, "Unraveling spatio-temporal climatic patterns via multi-scale complex networks," Ph.D. thesis (University of Potsdam, 2019).
[41]J. Heitzig, J. F. Donges, Y. Zou, N. Marwan, and J. Kurths, "Node-weighted measures for complex networks with spatially embedded, sampled, or differently sized nodes," Eur. Phys. J. B **85**(1), 38 (2012).
[42]N. J. Mantua and S. R. Hare, "The pacific decadal oscillation," J. Oceanography **58**(1), 35–44 (2002).
[43]S.-W. Yeh, W. Cai, S.-K. Min, M. J. McPhaden, D. Dommenget, B. Dewitte, M. Collins, K. Ashok, S.-I. An, B.-Y. Yim, and J.-S. Kug, "Enso atmospheric teleconnections and their response to greenhouse gas forcing," Rev. Geophys. **56**(1), 185–206, https://doi.org/10.1002/rog.v56.1 (2018).
[44]J. C. H. Chiang and D. J. Vimont, "Analogous pacific and atlantic meridional modes of tropical atmosphere–ocean variability," J. Clim. **17**(21), 4143–4158 (2004).
[45]E. Di Lorenzo, G. Liguori, N. Schneider, J. C. Furtado, B. T. Anderson, and M. A. Alexander, "Enso and meridional modes: A null hypothesis for pacific climate variability," Geophys. Res. Lett. **42**(21), 9440–9448, https://doi.org/10.1002/2015GL066281 (2015).
[46]R. C. Wills, T. Schneider, J. M. Wallace, D. S. Battisti, and D. L. Hartmann, "Disentangling global warming multidecadal variability, and El Niño in pacific temperatures," Geophys. Res. Lett. **45**(5), 2487–2496, https://doi.org/10.1002/grl.v45.5 (2018).
[47]Y. Y. S. Yiu, "El Niño Southern Oscillation teleconnections and their effects on the Amundsen Sea region," Thesis (University of Cambridge, 2018).
[48]J. C. Rogers and H. van Loon, "Spatial variability of sea level pressure and 500 mb height anomalies over the Southern Hemisphere," Monthly Weather Rev. **110**(10), 1375–1392 (1982).
[49]J. S. Risbey, M. J. Pook, P. C. McIntosh, M. C. Wheeler, and H. H. Hendon, "On the remote drivers of rainfall variability in Australia," Monthly Weather Rev. **137**(10), 3233–3253 (2009).
[50]N. P. Gillett, T. D. Kell, and P. D. Jones, "Regional climate impacts of the Southern annular mode," Geophys. Res. Lett. **33**(23), L23704, https://doi.org/10.1029/2006GL027721 (2006).
[51]Z. Wu, J. Li, B. Wang, and X. Liu, "Can the Southern Hemisphere annular mode affect China winter monsoon?," J. Geophys. Res., [Atmos.] **114**(D11), D11107, https://doi.org/10.1029/2008JD011501 (2009).
[52]M. E. Linkin and S. Nigam, "The North Pacific Oscillation–West Pacific teleconnection pattern: Mature-phase structure and winter impacts," J. Clim. **21**(9), 1979–1997 (2008).
[53]S.-J. Shin and S.-I. An, "Interdecadal change in the relationship between the North Pacific Oscillation and the Pacific meridional mode and its impact on ENSO," Asia-Pacific J. Atmos. Sci. **54**(1), 63–76 (2018).
[54]L. Wang and W. Chen, "An intensity index for the East Asian winter monsoon," J. Clim. **27**(6), 2361–2374 (2014).
[55]M. N. Raphael, G. J. Marshall, J. Turner, R. L. Fogt, D. Schneider, D. A. Dixon, J. S. Hosking, J. M. Jones, and W. R. Hobbs, "The Amundsen Sea low: Variability, change, and impact on Antarctic climate," Bull. Am. Meteorol. Soc. **97**(1), 111–121 (2016).
[56]N. H. Saji, B. N. Goswami, P. N. Vinayachandran, and T. Yamagata, "A dipole mode in the tropical Indian Ocean," Nature **401**(6751), 360–363 (1999).
[57]P. J. Webster, A. M. Moore, J. P. Loschnigg, and R. R. Leben, "Coupled ocean-atmosphere dynamics in the Indian Ocean during 1997–98," Nature **401**(6751), 356–360 (1999).
[58]S. C. Chan, S. K. Behera, and T. Yamagata, "Indian Ocean dipole influence on South American rainfall," Geophys. Res. Lett. **35**(14), L14S12, https://doi.org/10.1029/2008GL034204 (2008).
[59]N. Singhrattna, B. Rajagopalan, M. Clark, and K. Krishna Kumar, "Seasonal forecasting of Thailand summer monsoon rainfall," Int. J. Climatol. **25**(5), 649–664 (2005).
[60]Y. Qiu, W. Cai, X. Guo, and B. Ng, "The asymmetric influence of the positive and negative IOD events on China's rainfall," Sci. Rep. **4**, 4943 (2014).
[61]C. J. C. Reason, "Subtropical Indian Ocean SST dipole events and southern African rainfall," Geophys. Res. Lett. **28**(11), 2225–2227, https://doi.org/10.1029/2000GL012735 (2001).
[62]J. F. Lübbecke, B. Rodríguez-Fonseca, I. Richter, M. Marín-Rey, T. Losada, I. Polo, and N. S. Keenlyside, "Equatorial Atlantic variability—modes, mechanisms, and global teleconnections," Wiley Interdiscip. Rev. Clim. Change **9**(4), e527 (2018).
[63]E. Mohino and T. Losada, "Impacts of the Atlantic equatorial mode in a warmer climate," Clim. Dyn. **45**(7), 2255–2271 (2015).
[64]T. Losada, B. Rodríguez-Fonseca, S. Janicot, S. Gervois, F. Chauvin, and P. Ruti, "A multi-model approach to the Atlantic equatorial mode: Impact on the West African monsoon," Clim. Dyn. **35**(1), 29–43 (2010).
[65]A. Giannini, R. Saravanan, and P. Chang, "The preconditioning role of tropical Atlantic variability in the development of the ENSO teleconnection: Implications for the prediction of Nordeste rainfall," Clim. Dyn. **22**(8), 839–855 (2004).
[66]J. García-Serrano, T. Losada, and B. Rodríguez-Fonseca, "Extratropical atmospheric response to the Atlantic Niño decaying phase," J. Clim. **24**(6), 1613–1625 (2011).
[67]A. Perinelli, D. E. Chiari, and L. Ricci, "Correlation in brain networks at different time scale resolution," Chaos **28**(6), 063127 (2018).
[68]K. Gupta and G. Ambika, "Role of time scales and topology on the dynamics of complex networks," e-print arXiv:1810.00687 (2018).
[69]J. F. Donges, J. Heitzig, B. Beronov, M. Wiedermann, J. Runge, Q. Y. Feng, L. Tupikina, V. Stolbova, R. V. Donner, N. Marwan, H. A. Dijkstra, and J. Kurths, "Unified functional network and nonlinear time series analysis for complex systems science: The pyunicorn package," Chaos **25**(11), 113101 (2015).